

Comparative Resonant Inelastic X-ray Scattering Study of Ca_2RuO_4 and $\text{Ca}_3\text{Ru}_2\text{O}_7$

K. von Arx,¹ F. Forte,^{2,3} M. Horio,¹ V. Granata,^{2,3} Q. Wang,¹ L. Das,¹ Y. Sassa,⁴ R. Fittipaldi,^{2,3} C. G. Fatuzzo,^{5,1,*} O. Ivashko,^{1,†} Y. Tseng,⁶ E. Paris,⁶ A. Vecchione,^{2,3} T. Schmitt,⁶ M. Cuoco,^{2,3} and J. Chang¹

¹*Physik-Institut, Universität Zürich, Winterthurerstrasse 190, CH-8057 Zürich, Switzerland*

²*CNR-SPIN, I-84084 Fisciano, Salerno, Italy*

³*Dipartimento di Fisica “E.R. Caianiello”, Università di Salerno, I-84084 Fisciano, Salerno, Italy*

⁴*Department of Physics, Chalmers University of Technology, SE-412 96 Gothenburg, Sweden*

⁵*Institute of Physics, École Polytechnique Fédérale de Lausanne (EPFL), CH-1015 Lausanne, Switzerland*

⁶*Swiss Light Source, Photon Science Division, Paul Scherrer Institut, CH-5232 Villigen PSI, Switzerland*

We present a combined oxygen K -edge x-ray absorption spectroscopy (XAS) and resonant inelastic x-ray scattering (RIXS) study of the bilayer ruthenate $\text{Ca}_3\text{Ru}_2\text{O}_7$. Our RIXS experiments on $\text{Ca}_3\text{Ru}_2\text{O}_7$ were carried out on the overlapping in-plane and inner apical oxygen resonances, which are distinguishable from the outer apical one. Comparison to equivalent oxygen K -edge spectra recorded on band-Mott insulating Ca_2RuO_4 is made. In contrast to Ca_2RuO_4 spectra, which contain excitations linked to Mott physics, $\text{Ca}_3\text{Ru}_2\text{O}_7$ spectra feature only intra- t_{2g} ones that do not directly involve the Coulomb energy scale. As found in Ca_2RuO_4 , we resolve two intra- t_{2g} excitations in $\text{Ca}_3\text{Ru}_2\text{O}_7$. Moreover, the lowest lying excitation in $\text{Ca}_3\text{Ru}_2\text{O}_7$ shows a significant dispersion, revealing a collective character differently from what is observed in Ca_2RuO_4 . Theoretical modelling supports the interpretation of this lowest energy excitation in $\text{Ca}_3\text{Ru}_2\text{O}_7$ as a magnetic transverse mode with multi-particle character, whereas the corresponding excitation in Ca_2RuO_4 is assigned to combined longitudinal and transverse spin modes. These fundamental differences are discussed in terms of the inequivalent magnetic ground-state manifestations in Ca_2RuO_4 and $\text{Ca}_3\text{Ru}_2\text{O}_7$.

I. INTRODUCTION

Transition metal (TM) oxides with $4d$ valence electrons often exhibit unconventional magnetic and electronic properties. These are dictated by the competition of comparable energy scales set by local interactions, including the Hund’s rule and crystal field (CF) terms, together with intrinsic spin-orbit coupling (SOC) of TM ions. By entangling the electron spin to the shape of the electronic cloud in the crystal, SOC makes the electronic spin-orbital states highly sensitive to the inter-site connectivity and effective dimensionality of the underlying lattice. One of the most important consequences is the possibility to tune the relative strength of competing magnetic interactions by varying the effective dimensionality in layered materials. Calcium-based ruthenates of the Ruddlesden-Popper family $\text{Ca}_{n+1}\text{Ru}_n\text{O}_{3n+1}$ offer one of the richest playgrounds with a great variety of phenomenology. The bilayer compound $\text{Ca}_3\text{Ru}_2\text{O}_7$ and its derivatives have been the subject of intense investigations due to a multitude of interesting low-temperature properties, such as spin-valve and giant magnetoresistance effects^{1–7}. It has been established that $\text{Ca}_3\text{Ru}_2\text{O}_7$ undergoes a magnetic transition at $T_N = 56$ K and an electronic transition at $T_s = 48$ K^{8–10}. The latter transition is sometimes referred to as a metal-insulator transition even though the system remains (semi) metallic down to base temperature^{9,10}. Those referring to a metal-insulator transition are probably motivated by the steep up-rise of the out-of-plane resistivity ρ_c ⁴. Another reason is the lattice response across T_s . Cooling below T_s generates a c -axis lattice parameter compression and, through the Poisson’s relation, an in-plane lattice parameter enhancement¹¹. This resembles what happens at

the metal-insulator transition (350 K) of Ca_2RuO_4 ^{12,13}. There, the c -axis compression leads to an almost fully occupied d_{xy} orbital and a Mott-gap opening in the half-filled d_{xz} and d_{yz} bands. However, the effect in $\text{Ca}_3\text{Ru}_2\text{O}_7$ is much smaller (0.1% and >1% compression of the lattice parameter c in $\text{Ca}_3\text{Ru}_2\text{O}_7$ and Ca_2RuO_4 , respectively)^{11,14}. The fact that both $\text{Ca}_3\text{Ru}_2\text{O}_7$ and Ca_2RuO_4 undergo similar c -axis compressive transitions but end up with different ground states makes comparative studies interesting. In addition to the electronic properties, the magnetic ground states of these two compounds differ as well. Whereas Ca_2RuO_4 displays a G-type antiferromagnetic state below $T_N = 110$ K¹⁵, the in-plane magnetic moments in $\text{Ca}_3\text{Ru}_2\text{O}_7$ order ferromagnetically, leading to an A-type antiferromagnetic state¹¹. This difference in the in-plane magnetic order implies that the interaction within the layers plays an important role for the magnetic ground state of these compounds. The investigation of the magnetic and orbital degrees of freedom and their excitation spectrum therefore offers a view on the complex interplay between different energy scales relevant for the ground state. In this respect, recent spectroscopic and neutron scattering measurements demonstrated that the magnetic ordering in Ca_2RuO_4 may sustain both longitudinal and transverse magnon modes with a large anisotropy gap, which reflects the impact of broken tetragonal symmetry in combination with SOC^{16–18}.

In this paper, we present a combined oxygen K -edge x-ray absorption spectroscopy (XAS) and resonant inelastic x-ray scattering (RIXS) study of $\text{Ca}_3\text{Ru}_2\text{O}_7$ and compare it to previously published work on Ca_2RuO_4 ^{18,19}, with the aim to investigate the distinctive fingerprints of the magnetic state in the single and bilayer compounds.

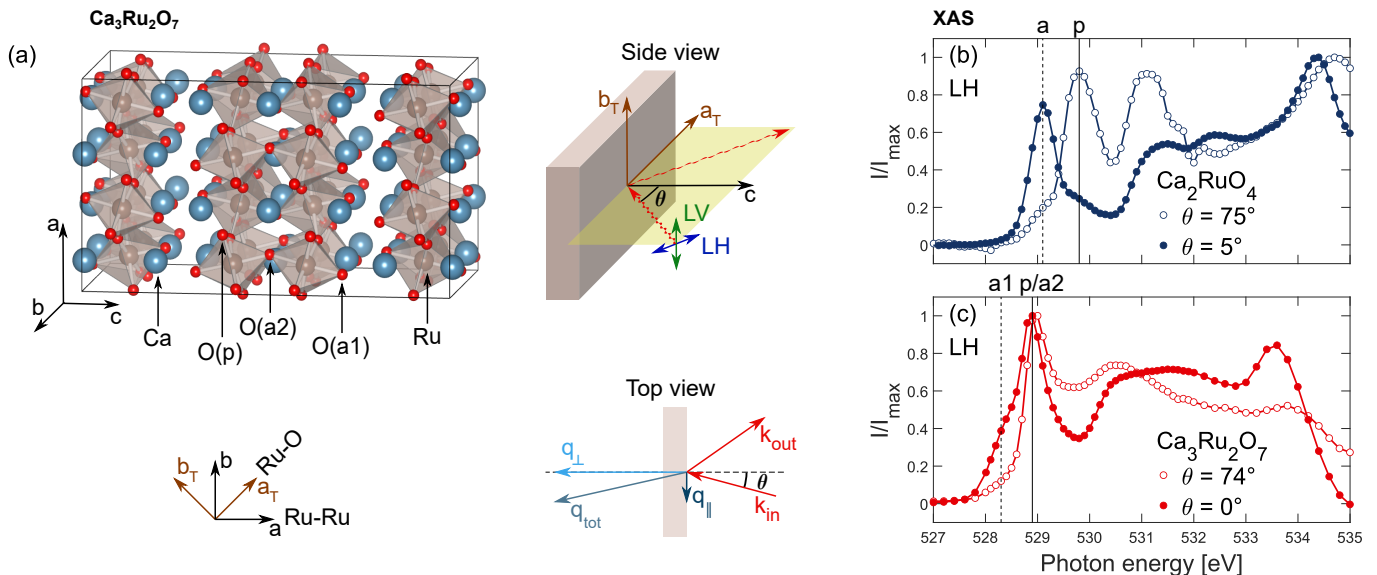


FIG. 1. (a) Schematically depicted RIXS geometry with respect to the crystal lattice of $\text{Ca}_3\text{Ru}_2\text{O}_7$. Different oxygen sites in the crystal structure are labelled as O(p), O(a1) and O(a2) for planar, outer apical and inner apical sites, respectively. Momentum dependence was measured along the Ru-O direction. Therefore, the reciprocal space is indexed in tetragonal notation with $a_T \approx b_T \approx 1/2\sqrt{a^2 + b^2}$, where $a = 5.37 \text{ \AA}$ and $b = 5.54 \text{ \AA}$ ¹¹. (b), (c) Background subtracted and normalized XAS spectra of Ca_2RuO_4 and $\text{Ca}_3\text{Ru}_2\text{O}_7$, respectively. The spectra were recorded with LH polarization near grazing and normal incident light directions as indicated. The dashed vertical black line indicates apical (Ca_2RuO_4) and outer apical ($\text{Ca}_3\text{Ru}_2\text{O}_7$), whereas the solid vertical black line indicates planar (Ca_2RuO_4) and overlapping planar and inner apical ($\text{Ca}_3\text{Ru}_2\text{O}_7$) oxygen resonances probing Ru t_{2g} states. Dark blue data on Ca_2RuO_4 are taken from ref. 18.

With this methodology, the Ru $4d$ orbitals are accessed indirectly through their hybridization with oxygen p orbitals. This indirect approach has routinely been applied to different TM oxides^{20–23}.

Our study demonstrates that in $\text{Ca}_3\text{Ru}_2\text{O}_7$, only the two lowest intra- t_{2g} excitations are observed, whereas in Ca_2RuO_4 , the Mott insulating ground state produces a set of excitations within the t_{2g} subspace, which consists of two low-energy and two mid/high-energy structures. An important difference – the main observation reported here – is that the lowest lying excitation exhibits a clear dispersive character in $\text{Ca}_3\text{Ru}_2\text{O}_7$. This marked collective behavior is not found with the corresponding excitation in Ca_2RuO_4 . The fundamentally different magnetic ground states of Ca_2RuO_4 and $\text{Ca}_3\text{Ru}_2\text{O}_7$ are therefore manifested in the excitation spectrum, both within the t_{2g} and between the t_{2g} and e_g sectors. We discuss this within the theoretical framework of fast collision approximation for the RIXS cross-section^{24,25}. Taking into account the different magnetic ground states of Ca_2RuO_4 and $\text{Ca}_3\text{Ru}_2\text{O}_7$, qualitative agreement is obtained. Moreover, we analyze the nature of the lowest lying intra- t_{2g} excitation. In this fashion, we show that this excitation is magnetic in both compounds, but with fundamentally different natures. In Ca_2RuO_4 , the lowest lying excitation is consistent with composite longitudinal amplitude and transverse spin modes, whereas in $\text{Ca}_3\text{Ru}_2\text{O}_7$ it has a dominant transverse spin nature.

These results provide decisive evidence for the capa-

bility of oxygen K -edge RIXS in probing the complex structure of electronic excitations in $4d$ ruthenates. Particularly, it is confirmed that the low-energy spin/orbital modes are also directly accessible in virtue of modest SOC²². Such elementary excitations reflect the balance among competing interactions, being therefore crucial for revealing the origin of emergent phases and for determining the low-energy Hamiltonian in layered ruthenates, where magnetic interactions are no longer dictated by a global spin $\text{SU}(2)$ symmetry alone.

II. METHODS

High quality single crystals of $\text{Ca}_3\text{Ru}_2\text{O}_7$ were grown by the floating zone techniques^{26,27}, aligned *ex situ* by x-ray LAUE and cleaved *in situ* using the top-post method. XAS and RIXS²⁵ measurements were carried out at the ADDRESS beamline^{28,29} of the Swiss Light Source (SLS) at the Paul Scherrer Institut. The scattering geometry is indicated in Fig. 1(a). A fixed angle of 130° between incident and scattered light was used. In-plane momentum $\mathbf{q}_{\parallel} = (h, k)$ is varied by controlling the incident photon angle θ . In this work, the reciprocal space is indexed in tetragonal notation. Grazing and normal incidence conditions refer to $\theta \approx 90^\circ$ and 0° , respectively. Linear vertical (LV) and horizontal (LH) light polarizations were used to probe the oxygen K -edge at which an energy resolution of 22.5 meV (Gaussian standard deviation σ)

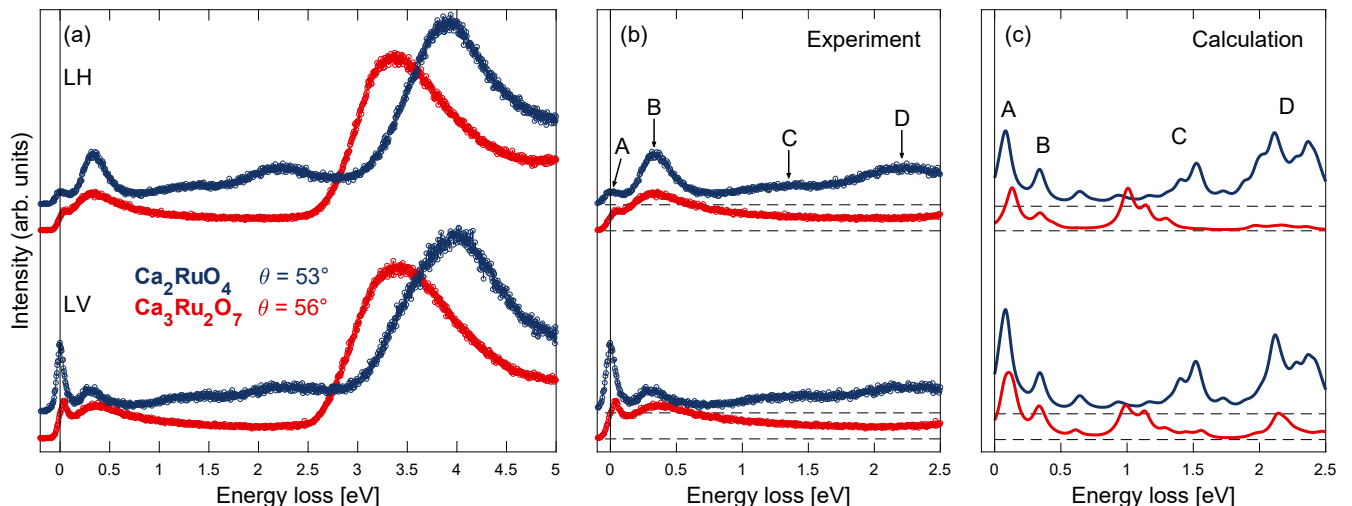


FIG. 2. (a) RIXS spectra of Ca_2RuO_4 and $\text{Ca}_3\text{Ru}_2\text{O}_7$ recorded with LH and LV polarization as indicated. To enhance visibility, the spectra are given an individual vertical shift. Dark blue data on Ca_2RuO_4 are taken from ref. 18. (b) Zoom of (a) to show the low-energy excitations labelled as A, B, C and D. (c) Calculated RIXS spectra of Ca_2RuO_4 and $\text{Ca}_3\text{Ru}_2\text{O}_7$ for LH and LV polarization.

was obtained. Elastic scattering throughout this work is modelled by a Gaussian lineshape with σ set by the energy resolution. The presented data is collected at the base temperature $T = 20$ K unless otherwise indicated.

III. RESULTS

The oxygen K -edge XAS spectra taken with LH light polarization on Ca_2RuO_4 and $\text{Ca}_3\text{Ru}_2\text{O}_7$ are shown in Figs. 1(b) and (c). For Ca_2RuO_4 , the apical and planar oxygen resonances are disentangled by using LH light near normal or grazing conditions respectively^{18,19}. The first and second pre-edges, indicated by dashed and solid vertical lines, correspond respectively to the resonances at the apical and planar oxygen sites, from which hybridization with Ru t_{2g} orbitals takes place. In the case of $\text{Ca}_3\text{Ru}_2\text{O}_7$, there are three oxygen sites: one planar O(p) and two apical, outer O(a1) and inner O(a2) – see Fig. 1(a). Compared to Ca_2RuO_4 , these oxygen sites are harder to distinguish in the XAS spectra of $\text{Ca}_3\text{Ru}_2\text{O}_7$ as the O(p) and O(a2) sites have similar CF environments. Similarly to other layered oxides^{21,30}, we assign the first pre-edge of $\text{Ca}_3\text{Ru}_2\text{O}_7$ to the O(a1) site. In the normal ($\theta = 0^\circ$) condition, this resonance appears as a shoulder (528.3 eV) on the second pre-edge (528.9 eV) that is assigned to the O(p) and O(a2) sites. The reduced splitting of the oxygen K -pre-edges is also known from the XAS study of the Ruddlesden-Popper $\text{Sr}_{1+n}\text{Ru}_n\text{O}_{3n+1}$ series with $n = 1, 2$, and 3^{31,32}. Eventually, for cubic SrRuO_3 , the two pre-edges merge together and only one feature is observed³³. The features at higher energies correspond to resonances probing the O p orbitals hybridized with the unoccupied Ru e_g states.

For our RIXS study of $\text{Ca}_3\text{Ru}_2\text{O}_7$, we have focused en-

tirely on the most intense oxygen K -pre-edge that probes the planar and inner apical sites. In Figs. 2(a) and (b), spectra recorded with LV and LH light are compared to the corresponding planar spectra of Ca_2RuO_4 . First, we notice that the “block” of dd -excitations in $\text{Ca}_3\text{Ru}_2\text{O}_7$ around 3.5 eV is consistently shifted to lower energies relatively to what is found in Ca_2RuO_4 . Another noticeable difference is that among the four “low” energy excitations reported¹⁸ for Ca_2RuO_4 [labelled as A, B, C, and D in Fig. 2(b)], only the two lowest (A and B) are found in $\text{Ca}_3\text{Ru}_2\text{O}_7$. The B excitation of bilayer $\text{Ca}_3\text{Ru}_2\text{O}_7$ has a significantly smaller amplitude and is much broader than in Ca_2RuO_4 . However, for both compounds, the B excitation is more intense when probed with LH polarization, see Fig. 3(a).

The lowest lying excitation (labelled as A) is overlapping with the elastic line and careful analysis is required to separate these two contributions. Elastic scattering is most pronounced near the specular condition, therefore the A excitation appears as a shoulder on the energy loss side – see Fig. 3(b). Near grazing condition, the situation is reversed and the elastic scattering appears as a shoulder on the left side of the A excitation peak. To model the elastic contribution, we use a Gaussian profile with the linewidth set by the energy resolution. In this fashion, it is possible to extract the A excitation by subtracting the elastic component as well as the contributions from the B excitation and background, as illustrated in Figs. 3(b) and (c). As the incidence angle – and hence the in-plane momentum transfer – is varied, the A excitation is dispersing to a lower energy away from the zone center. Finally, the A excitation persists at least up to 80 K, as shown in Fig. 3(c).

The momentum dependence of the A and B excitations extracted from the $\text{Ca}_3\text{Ru}_2\text{O}_7$ data are compared

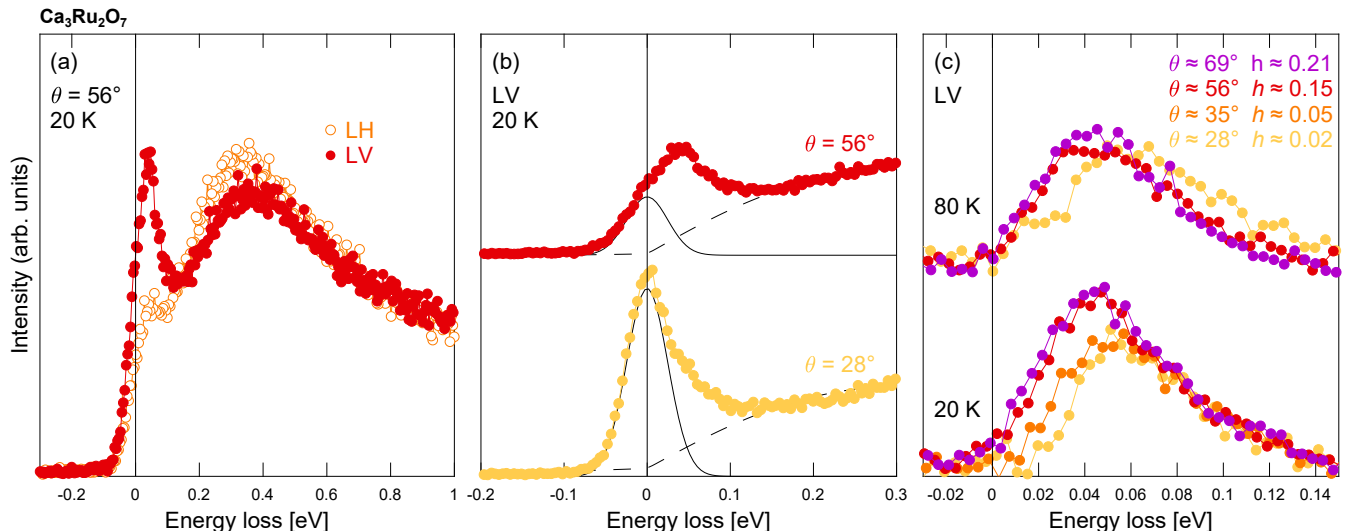


FIG. 3. RIXS spectra of $\text{Ca}_3\text{Ru}_2\text{O}_7$ focusing on the low-energy part. (a) Comparison between LH and LV spectra at the same incidence angle. (b) Low-energy part for two different incidence angles measured with LV polarization. Solid black lines are Gaussian fits with a width fixed to the energy resolution of the experiment to model the elastic scattering. Dashed black lines are the sums of B excitation and background contributions. To enhance visibility, the spectrum at higher angle is given a vertical shift. (c) RIXS spectra after subtraction of the elastic line, B excitation and background contributions to show the dispersion of the A excitation at 20 K and 80 K, as indicated. To enhance visibility, the spectra at 80 K are given a vertical shift. The indicated θ and h values correspond to the 20 K data, values for 80 K data differ slightly – see Fig. 4.

in Fig. 4 to the corresponding excitations in Ca_2RuO_4 . For the B excitation, the peak position is defined as the maximum obtained from the derivative of the spectrum, since the peak is extremely broad. Within the energy resolution of this experiment, no momentum dependence can be resolved for this excitation in $\text{Ca}_3\text{Ru}_2\text{O}_7$. The situation is different in Ca_2RuO_4 , where a small upward dispersion away from the zone center is detected for the B excitation¹⁸. Most pronounced differences are observed for the A excitation. The strong dispersion found in $\text{Ca}_3\text{Ru}_2\text{O}_7$ is completely absent in Ca_2RuO_4 . Additionally, the excitation is located at significantly higher energies in Ca_2RuO_4 at around 80 meV compared to 55 meV in $\text{Ca}_3\text{Ru}_2\text{O}_7$.

IV. DISCUSSION

To discuss the XAS spectra, we first summarize the interpretation of the Ca_2RuO_4 data published recently^{18,19}. The exact mechanism behind the Mott insulating state of Ca_2RuO_4 has long been under discussion and various theoretical models have been proposed^{34–36}. In this context, the Ca_2RuO_4 XAS results strongly support the explanation via a complete orbital polarization with the almost fully occupied d_{xy} orbital. Indeed, the XAS spectra, shown in Fig.1(b), are in perfect accordance with this picture. For example, near normal incidence, the LH polarized light promotes a core electron into the O p_x orbital that hybridizes with Ru d_{xz} orbitals at the apical and Ru d_{xy} orbitals at the planar

site. Because the fully occupied Ru d_{xy} orbital is not available for absorption, the intensity at this resonance is strongly suppressed and a pronounced response is only observed at the apical oxygen resonance. For near grazing incidence the situation is reversed and the stronger XAS response flips to the planar resonance. Comparing the Ca_2RuO_4 and $\text{Ca}_3\text{Ru}_2\text{O}_7$ spectra, the differences in crystal structure and orbital occupation become apparent. Due to the two nonequivalent apical oxygen sites in $\text{Ca}_3\text{Ru}_2\text{O}_7$, the apical feature splits and the outer apical one is only visible as a shoulder to the strong planar resonance that overlaps with the inner apical resonance. Taking into account the relative intensities of the two features, the XAS results suggest a different orbital occupation than in Ca_2RuO_4 , with an only partially filled d_{xy} . This partial occupation is also in accordance with the reduced c -axis compression in $\text{Ca}_3\text{Ru}_2\text{O}_7$ compared to Ca_2RuO_4 ^{11,14}.

Next, we turn to discuss the RIXS spectra. The fact that completely different oxygen K -edge RIXS spectra are observed for Ca_2RuO_4 and $\text{Ca}_3\text{Ru}_2\text{O}_7$ is a beautiful example of how ground state fingerprints are encoded into the excitations. In principle, the CF environment around an in-plane oxygen should be similar for Ca_2RuO_4 and $\text{Ca}_3\text{Ru}_2\text{O}_7$. Yet, the RIXS excitation spectra are fundamentally different for these two compounds. In Ca_2RuO_4 , a sequence of excitations has been identified in the t_{2g} sector, which are separated from the higher energy $t_{2g} \rightarrow e_g$ features in the energy range ~ 3 –5 eV^{18,38} – see Fig. 2(a). In particular, two broad excitations located around 1 eV and 2 eV, labelled as C

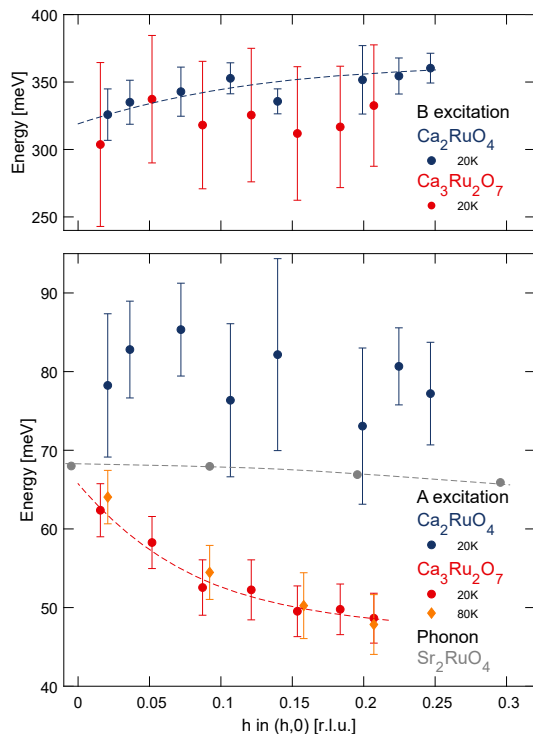


FIG. 4. Dispersion of the low-energy excitations along θ which corresponds to a varying in plane momentum $\mathbf{q} = (h, 0)$ for the A (bottom) and B (top) excitations. Errorbars for the A excitation in $\text{Ca}_3\text{Ru}_2\text{O}_7$ indicate standard deviation 3σ of the fitted peak position. By contrast, for the B excitation, the errorbars reflect the peak width at 98% of the total height. Dark blue data show the dispersion for the single layer Ca_2RuO_4 , taken from ref. 18 including error bars. Grey data show a phonon dispersion in Sr_2RuO_4 measured by inelastic neutron scattering³⁷. Dashed lines are guides to the eye.

and D, are linked to the energy scales of Hund’s coupling and Coulomb interaction responsible for the Mott insulating ground state. In semi-metallic $\text{Ca}_3\text{Ru}_2\text{O}_7$ by contrast, these excitations are completely absent – see Fig. 2(b). Even within the lower energy t_{2g} sector, pronounced differences are identified. Although two excitations (labelled as A and B) – with similar energy scales – are resolved for both compounds, they appear to have a fundamentally different nature. In $\text{Ca}_3\text{Ru}_2\text{O}_7$ the lowest lying excitation is clearly dispersive, whereas in Ca_2RuO_4 no dispersion was resolved for the corresponding branch.

To gain insight into the microscopic picture behind these excitations, the RIXS response was modelled for both compounds, and compared to the experimental spectra in Fig. 2. We used the fast collision approximation^{24,25} of the RIXS cross-section describing the light-induced excitation – and subsequent absorption – of an electron from the O 1s level into the 2p level, for both LV and LH incoming polarization. Full detailed description of this approach is reported in Appendices A and B. The RIXS intensity was calculated via exact diago-

nalization of a model Hamiltonian defined on a cluster of two ruthenium sites connected by one planar oxygen site along an in-plane direction. The bond bending due to the rotation of the octahedra around the c axis is allowed. The ruthenium-site Hamiltonian is defined on the t_{2g} subspace and consists of three terms: (1) CF splitting Δ between the d_{xy} and d_{xz} , d_{yz} orbitals, (2) SOC λ , and (3) Coulomb interaction, which is expanded into intra-orbital and inter-orbital Hubbard interactions of strengths U and $(U - 5J_H/2)$, respectively. Inter-orbital Hund’s coupling as well as the pair-hopping term, are both of strength J_H . Material specific values $\Delta = 0.3$ eV, $\lambda = 0.05$ eV, $U = 2.0$ eV, and $J_H = 0.4$ eV^{19,39–41}, are used to evaluate the model for both Ca_2RuO_4 and $\text{Ca}_3\text{Ru}_2\text{O}_7$. Similar values of Δ , U and J_H have been used for DMFT calculations⁴² of Ca_2RuO_4 and are comparable to those used in modelling the spin-excitation dispersion observed by neutron scattering¹⁶, RIXS spectra¹⁸, as well as magnetic anisotropy⁴³. Here, we point out that small differences from previous estimates of the microscopic parameters are fully awaited since, in our description, the oxygen degrees of freedom are explicitly included, and this may lead to a renormalization of the local interaction terms. To take into account the different ground states, Ca_2RuO_4 is modelled with an antiferromagnetic (AFM) in-plane interaction, whereas we consider an extra exchange field to stabilize the ferromagnetic (FM) ground state and spins along the in-plane easy axis in $\text{Ca}_3\text{Ru}_2\text{O}_7$ ^{11,15}. Henceforth, we will also refer to the Ca_2RuO_4 and $\text{Ca}_3\text{Ru}_2\text{O}_7$ bonds as AFM and FM, respectively, corresponding to the G-type and A-type AFM structures.

In Fig. 2(c) the calculated RIXS responses in LH and LV polarizations are presented for both ground states, showing a good overall agreement with the experimental spectra in Fig. 2(b). In both cases four distinct excitations are evident, with approximate energy losses of 0.08, 0.4, 1–1.5 and 2 eV. In the FM case, we observe an overall decrease of the peak intensities. This effect is even more pronounced for excitations above 1 eV.

The origin of the four features for Ca_2RuO_4 has already been assigned in a previous work, and we recall it here for convenience¹⁸. We point out that, in the present simulation, the RIXS intensity has been evaluated by fully taking into account the scattering geometry in Fig. 1(a), and that the LV and LH spectra have been obtained by averaging the spectra over two orthogonal in-plane bond directions of the cluster.

Excitations A, B, C, and D in Ca_2RuO_4 have been interpreted on the basis of the multiplet structure of the d^4 configuration of the Ru^{4+} ion. In particular, they are associated to transitions within low-energy spin-orbital configurations, which have one doubly occupied orbital (doublon), or two doubly occupied orbitals. In the framework of the ionic picture, structures C and D have been assigned to J_H driven spin-state transitions between $S = 1$ and $S = 0$ states in the single- and two-doublon sectors¹⁸. The suppression of the weight asso-

ciated to the features above 1 eV in the case of a FM configuration is a consequence of the Pauli blocking of those intra- t_{2g} transitions. This mechanism may justify the lowered intensity of C and D structures in the FM background of Ru-O planes in $\text{Ca}_3\text{Ru}_2\text{O}_7$.

In Ca_2RuO_4 , the lowest energy features A and B are associated to spin-orbital excitations within the $S = 1$ subspace of the t_{2g} multiplets, whose energies are determined by the relative strength of the CF potential and the SOC. Even though they are not fully resolved experimentally due to limited energy resolution, those excitations are accessible in oxygen K -edge because of the SOC in the Ru $4d$ shell which strongly hybridizes $4d$ states with O $2p$ orbitals. In particular, the B structure has been attributed to multiple transitions to the highest energy $S = 1$ spin-orbital sector, while the A structure has been generically associated to composite magnetic transitions within the lowest-energy sector. We observe that, in the FM case, features occurring at a similar energy scale are observed, and we want to elucidate the possible spin-orbital (magnetic) origin of these excitations, with a special focus on the lowest A feature.

Beforehand, we observe that the lowest lying excitation A has an energy scale typical of both optical phonons and magnons. The strong dispersion of this excitation near the zone center is, however, atypical for optical phonons. In Sr_2RuO_4 , where complete phonon dispersions have been calculated and probed by neutron scattering^{37,44}, optical phonons are in fact found at ~ 70 and ~ 90 meV. None of them has a dispersion around the zone center compatible with what we observe in $\text{Ca}_3\text{Ru}_2\text{O}_7$. This is demonstrated in Fig. 4, where the relevant optical Sr_2RuO_4 phonon dispersion – measured by neutron scattering – is shown in grey. In comparison to the A excitation measured in $\text{Ca}_3\text{Ru}_2\text{O}_7$, this optical phonon is non-dispersive. Moreover, the 70 meV optical phonon found in Sr_2RuO_4 stems from vibrations of the apical oxygen whereas we are probing on the in-plane oxygen site. On this basis, assigning a magnetic origin to the lowest lying excitation appears the most plausible interpretation. We stress that it is not unusual to observe magnetic excitations beyond the magnetic ordered state due to the persistence of short-range magnetic correlations. In cuprates and iron pnictides, paramagnon excitations are found deep into the magnetically disordered state^{45–47}. Observing no significant temperature dependence of the A excitation dispersion is therefore expected.

To further verify the magnetic origin of the A excitations in Ca_2RuO_4 and $\text{Ca}_3\text{Ru}_2\text{O}_7$, and to reveal their distinct nature, we evaluated the dynamic spin structure factors $S^\mu(\mathbf{q}, \omega)$, and spin-spin dynamic spin structure factors $(S_i \cdot S_{i+1})^\mu(\mathbf{q}, \omega)$, $\mu = x, y, z$, [Fig. 5(b),(c),(e),(f)] for $\mathbf{q} = (0, 0)$ and $(\pi, 0)$, which are the only viable values for the momentum transfer of our Ru-O-Ru cluster. Here, we point out that the ground state is made by magnetic moments that are aligned in the Ru plane. For convenience, we refer to \parallel, \perp, z , for a spin mode excitation that is collinear, perpendicular in-plane, perpendicular

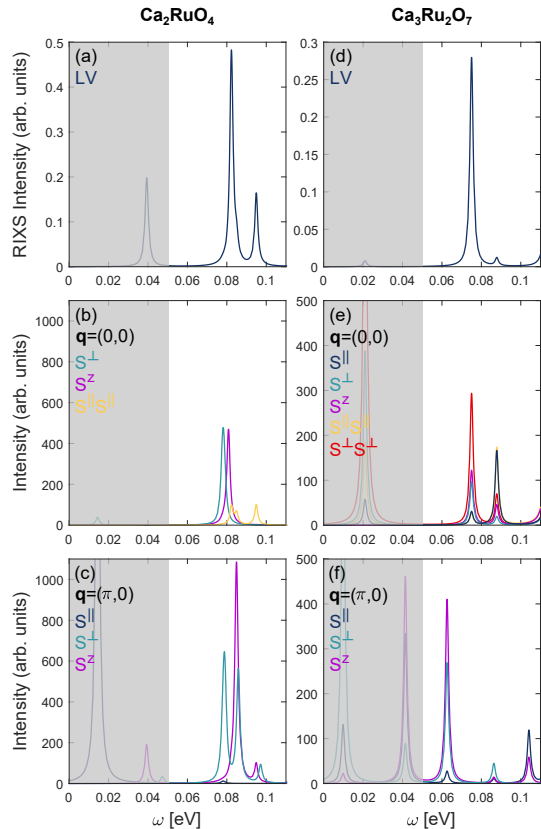


FIG. 5. Theoretical model calculation of the RIXS spectra in panels (a) and (d) and the dynamic spin structure factors $S^\mu(\mathbf{q}, \omega)$, and spin-spin dynamic spin structure factors $(S_i \cdot S_{i+1})^\mu(\mathbf{q}, \omega)$, $\mu = \parallel, \perp, z$, for $\mathbf{q} = (0, 0)$ and $(\pi, 0)$ in the low energy regime for Ca_2RuO_4 and $\text{Ca}_3\text{Ru}_2\text{O}_7$. The gray shaded area corresponds to the energy region currently not accessible by RIXS due to the limited resolution.

ular out-of-plane with respect to the orientation of the ordered magnetic moments in the ground state, respectively.

Let us start with the AFM case in Fig. 5(a)–(c). The comparison of the low-energy part of the RIXS spectrum for the AFM configuration with the calculated spin structure factors at $\mathbf{q} = (0, 0)$ allows to associate the dominant excitation in the RIXS spectrum to features with transverse single spin modes, i.e. S^z and S^\perp , and longitudinal two-spin $S^\parallel S^\parallel$ correlation functions. This is consistent with the previous interpretation of the A excitation as evidence of composite excitations such as longitudinal (Higgs) two-particle and transverse bimagnon modes^{17,18}. In particular, from the analysis we observe that the lowest energy spin excitations occur at about 20 and 40 meV – see Fig. 5(b),(c), mainly through single spin flip at each Ru site. The former energy scale is related to the effective single ion anisotropy due to the interplay of spin-orbit and crystal field potential. A distinctive aspect of the magnetic ground state is that, due to the spin-orbit coupling and crystal field potential, there is neither

rotational nor parity conservation for the local spin. The resulting ground state is then a quantum superposition of several components. Specifically, it consists of dominant exchange driven anisotropic antiferromagnetic correlations, and it also includes states corresponding to the variation of amplitude and direction of the local $S = 1$ magnetic moments with respect to the easy axis. This peculiar character of the ground state allows to have a significant spectral weight associated to high-energy excitations, corresponding to the RIXS active states close to 80 meV – see Fig. 5(a). Taking into account the energy profile of the dynamic spin response, we deduce that the modes at about 80 meV have a multi-particle spin character, as they are accessible by means of both single transverse and double longitudinal spin excitations. Our results also predict the existence of a lower energy feature in the RIXS spectrum, having similar character, at 40 meV, in an energy range which is not detectable in the present experiment.

The FM case offers a similar result, since the lowest A feature may also be associated to magnetic excitations. Notably in this case, the dominant excitation occurs at slightly lower energy, and corresponds to mainly transverse spin excitations, of single- S^z and S^\perp or two-particle type $S^\perp S^\perp$. Moreover, according to the simulation, the existence of a very weak feature located at 20 meV is also predicted.

Having identified the nature of the magnetic excitations associated to the lowest RIXS feature in both the AFM and FM ground states, one can also estimate the bandwidth of the continuum of the corresponding collective modes propagating along the $(0, 0) \rightarrow (\pi, 0)$ path. Comparing the relevant $S^\mu(\mathbf{q}, \omega)$ at $\mathbf{q} = (\pi, 0)$ and $(0, 0)$ shows that, in the AFM case, magnetic peaks are located approximately in the same energy range at different wave vectors. On the contrary, in the FM configuration, the peaks associated to the single spin excitations are shifted to lower energies by 20-30 meV, when going from $\mathbf{q} = (0, 0)$ to $\mathbf{q} = (\pi, 0)$. This is in accordance with what is observed in the experimental spectra – see Fig. 4. We also carried out the calculation of the local and two-site orbital angular momentum correlation functions, which reveal that the A peak in the AFM case has significant orbital contribution, while it is substantially suppressed in the FM case. This is consistent with the observation that the FM ground state has a different orbital pattern⁴⁸ when compared to the AFM configuration. The doublon can have a stronger tendency to occupy different orbitals on neighbouring Ru sites in the FM case. Moreover, the spin-orbit coupling tends to align the orbital moments; since the Ru spins are also ferromagnetically correlated. This implies that orbital variations can be suppressed in the low-energy spin sector. Here, we argue that the lack of the orbital component in the targeted excitation allows to have a larger effective exchange, which results in an enhancement of the bandwidth as we find in the cluster analysis.

V. CONCLUSIONS

In summary, we have carried out a combined oxygen K -edge XAS and RIXS study of $\text{Ca}_3\text{Ru}_2\text{O}_7$. Our results are compared to (i) equivalent experimental results previously obtained on single layer Ca_2RuO_4 and (ii) local cluster modelling of $\text{Ca}_3\text{Ru}_2\text{O}_7$ and Ca_2RuO_4 . In particular, the oxygen K -edge RIXS spectra are fundamentally different in $\text{Ca}_3\text{Ru}_2\text{O}_7$ and Ca_2RuO_4 , reflecting their different ground states. Whereas in Ca_2RuO_4 a set of excitations within the t_{2g} subspace, consisting of two low-energy and two mid/high-energy structures, is observed, only the two lowest intra- t_{2g} excitations have a significant amplitude in $\text{Ca}_3\text{Ru}_2\text{O}_7$. This effect is captured by the local cluster modelling taking into account the different in-plane magnetic couplings. Finally, we demonstrated that the lowest lying intra- t_{2g} excitation in $\text{Ca}_3\text{Ru}_2\text{O}_7$ is dispersing, revealing its collective origin. We argue based on the exact dispersion and comparison to spin correlation function computations, that this excitation is magnonic rather than phononic in nature. In fact, it is suggested to be dominantly a transverse mode with multi-particle character, which is indirectly allowed at the oxygen K -edge through substantial SOC of Ru ions.

VI. APPENDIX A: MODEL HAMILTONIAN

We report here the details of the microscopic model describing the energy levels and wave functions of the considered Ru-O-Ru cluster. The examined Hamiltonian^{49,50} is expressed as:

$$H = H_{kin} + H_{el-el} + H_{cf} + H_{soc} + H_m. \quad (1)$$

The first term in Eq. 1 is the kinetic operator describing the Ru-O connectivity:

$$H_{kin} = \sum_{ij, \alpha\beta, \sigma} t_{ij}^{\alpha\beta} (p_{i\alpha\sigma}^\dagger d_{j\beta\sigma} + h.c.), \quad (2)$$

where $d_{i\beta\sigma}^\dagger$ is the creation operator for an electron with spin σ at the i site in the β orbital of the t_{2g} sector (d_{xy} , d_{xz} , d_{yz}), while $p_{i\alpha\sigma}$ is the annihilation operator of an electron with spin σ at the i site in the α orbital of the (p_x , p_y , p_z) space of the oxygen. Hopping amplitudes $t_{ij}^{\alpha\beta}$ include all the allowed symmetry terms according to the Slater-Koster rules^{51,52} for a given bond connecting a ruthenium to an oxygen atom along, say, the x direction. We allow for the relative rotation of the oxygen octahedra surrounding the Ru site, assuming that the Ru-O-Ru bond can form an angle $\theta = (180^\circ - \phi)$. The case with $\phi = 0^\circ$ corresponds to the tetragonal undistorted bond, while a nonvanishing value of ϕ arises when the RuO_6 octahedra are rotated of the corresponding angle around the c axis.

The second term is the Coulomb interaction, which is expressed in terms of Kanamori parameters U , U' , and

J_H as follows

$$H_{el-el} = U \sum_{i\alpha} n_{i\alpha\uparrow} n_{i\alpha\downarrow} - 2J_H \sum_{i\alpha\beta} \mathbf{S}_{i\alpha} \cdot \mathbf{S}_{i\beta} +$$

$$(U' - \frac{J_H}{2}) \sum_{i\alpha \neq \beta} n_{i\alpha} n_{i\beta} + J' \sum_{i\alpha\beta} d_{i\alpha\uparrow}^\dagger d_{i\alpha\downarrow}^\dagger d_{i\beta\uparrow} d_{i\beta\downarrow} \quad (3)$$

where $n_{i\alpha\sigma}$, $\mathbf{S}_{i\alpha}$ are the on site charge for spin σ and the spin operators for the α orbital, respectively. U (U') is the intra (inter)-orbital Coulomb repulsion, J_H is the Hund coupling, and J' the pair hopping term. Due to the invariance for rotations in the orbital space, the following relations hold: $U = U' + 2J_H$, $J' = J_H$.

The H_{cf} part of the Hamiltonian H is the crystalline field potential, controlling the symmetry lowering from cubic to tetragonal one, due to the compression of RuO₆ octahedra along the c axis:

$$H_{cf} = \sum_i \Delta_i [n_{ixy} - \frac{1}{2}(n_{ixz} + n_{iyz})] \quad (4)$$

The SOC Hamiltonian reads as

$$H_{soc} = \lambda \sum_i \mathbf{L}_i \cdot \mathbf{S}_i. \quad (5)$$

Due to the cubic CF terms in RuO₆ octahedra separating the lower t_{2g} from the unoccupied e_g levels, \mathbf{L}_i stands for the angular momentum operator projected onto the t_{2g} subspace. Its components have the following expression in terms of orbital fermionic operators:

$$L_{ix} = i \sum_{\sigma} [d_{ixy\sigma}^\dagger d_{ixz\sigma} - d_{ixz\sigma}^\dagger d_{ixy\sigma}]$$

$$L_{iy} = i \sum_{\sigma} [d_{iyz\sigma}^\dagger d_{ixy\sigma} - d_{ixy\sigma}^\dagger d_{iyz\sigma}] \quad (6)$$

$$L_{iz} = i \sum_{\sigma} [d_{ixz\sigma}^\dagger d_{iyz\sigma} - d_{iyz\sigma}^\dagger d_{ixz\sigma}]$$

Finally, H_m in Eq. 1 is an effective exchange field which pins the magnetization at the Ru sites to be in the (x, y) plane for the FM ground state:

$$H_m = \sum_i \mathbf{S}_i \cdot \mathbf{B}_{xy}. \quad (7)$$

VII. APPENDIX B: CALCULATION OF THE RIXS CROSS SECTION

The RIXS intensity is described by the Kramers-Heisenberg relation

$$I(\omega, \mathbf{q}, \epsilon, \epsilon') = \sum_f |A_{fg}(\omega, \mathbf{q}, \epsilon, \epsilon')|^2 \delta(E_f + \omega_{k'} - E_g - \omega_k) \quad (8)$$

where $\omega = \omega_{k'} - \omega_k$ and $\mathbf{q} = \mathbf{k}' - \mathbf{k}$ stand for the energy and momentum transferred by the scattered photon, and ϵ and ϵ' for the incoming and outgoing light polarization vectors. We adopt the dipole and fast collision approximation, in which the RIXS scattering amplitude is reduced to

$$A_{fg} = \frac{1}{i\Gamma} \langle f | R(\epsilon, \epsilon', \mathbf{q}) | g \rangle, \quad (9)$$

where R is the effective RIXS scattering operator describing two subsequent dipole transitions, and Γ is the core-hole broadening. In the oxygen K -edge RIXS, the dipole transitions create an O $1s$ core hole and extra valence electron in a $2p$ orbital and viceversa, and the scattering operator has the following expression:

$$R(\epsilon_\nu, \epsilon_{\nu'}) \propto \sum_{i,\sigma} e^{i\mathbf{q}\cdot\mathbf{r}_i} p_{\nu'\sigma} p_{\nu\sigma}, \quad (10)$$

where ν is the (x, y, z) orbital and the sum over the different spin states is assumed. Matrix elements are then evaluated among oxygen valence states in Eq. 9. Notably, the valence electron in a $2p$ orbital hybridizes and interacts with the Ru d electrons.

In the adopted experimental scattering geometry, the dependence upon the incident angle θ_{in} and scattering angle $\alpha = 130^\circ$ between the incoming/outgoing polarization vectors is:

$$\epsilon_{LH} = \epsilon_x \cos \theta_{in} + \epsilon_z \sin \theta_{in}$$

$$\epsilon_{LV} = \epsilon_y \quad (11)$$

$$\epsilon' = \epsilon'_x \cos(\theta_{in} + \alpha) + \epsilon'_y + \epsilon'_z \sin(\theta_{in} + \alpha)$$

Here the coordinate frame (x, y, z) , corresponds to the tetragonal axis frame (a_T, b_T, c) . Since the outgoing polarization is not resolved, the RIXS intensity is obtained by summing up incoherently over all the three polarization directions $(\epsilon'_x, \epsilon'_y, \epsilon'_z)$.

VIII. ACKNOWLEDGEMENTS

The experimental work was performed at the ADDRESS beamline of the SLS at the Paul Scherrer Institut, Villigen PSI, Switzerland. We thank the ADDRESS beamline staff for technical support. K.v.A., M.H., Q.W, L.D., O.I., J.C. acknowledge support by the Swiss National Science Foundation. M.C. and F.F. acknowledge support by the project "Two-dimensional Oxides Platform for SPIN-orbitronics nanotechnology (TOPSPIN)" funded by the MIUR (PRIN) Bando 2017 - Grant 20177SL7HC. Y.S. is funded by the Swedish Research Council (VR) with a Starting Grant (No.2017-05078). Work at the Paul Scherrer Institut has been funded by the Swiss National Science Foundation through the Sinergia network Mott Physics Beyond the Heisenberg (MPBH) model (SNSF Research grant numbers CRSII2_141962 and CRSII2_160765).

- * Current address: Materials Sciences Division, Lawrence Berkeley National Laboratory, Berkeley, California 94720, USA
- † Current address: Deutsches Elektronen-Synchrotron DESY, 22607 Hamburg, Germany.
- 1 J. F. Karpus, R. Gupta, H. Barath, S. L. Cooper, and G. Cao, *Phys. Rev. Lett.* **93**, 167205 (2004).
 - 2 X. N. Lin, Z. X. Zhou, V. Durairaj, P. Schlottmann, and G. Cao, *Phys. Rev. Lett.* **95**, 017203 (2005).
 - 3 W. Bao, Z. Q. Mao, Z. Qu, and J. W. Lynn, *Phys. Rev. Lett.* **100**, 247203 (2008).
 - 4 N. Kikugawa, A. Winfried Rost, C. William Hicks, A. John Schofield, and A. Peter Mackenzie, *J. Phys. Soc. Jpn.* **79**, 024704 (2010).
 - 5 M. Zhu, J. Peng, T. Zou, K. Prokes, S. D. Mahanti, T. Hong, Z. Q. Mao, G. Q. Liu, and X. Ke, *Phys. Rev. Lett.* **116**, 216401 (2016).
 - 6 H. Xing, L. Wen, C. Shen, J. He, X. Cai, J. Peng, S. Wang, M. Tian, Z.-A. Xu, W. Ku, Z. Mao, and Y. Liu, *Phys. Rev. B* **97**, 041113(R) (2018).
 - 7 C. Sow, R. Numasaki, G. Mattoni, S. Yonezawa, N. Kikugawa, S. Uji, and Y. Maeno, *Phys. Rev. Lett.* **122**, 196602 (2019).
 - 8 G. Cao, L. Balicas, Y. Xin, J. E. Crow, and C. S. Nelson, *Phys. Rev. B* **67**, 184405 (2003).
 - 9 Y. Yoshida, I. Nagai, S.-I. Ikeda, N. Shirakawa, M. Kosaka, and N. Mōri, *Phys. Rev. B* **69**, 220411(R) (2004).
 - 10 E. Ohmichi, Y. Yoshida, S. I. Ikeda, N. Shirakawa, and T. Osada, *Phys. Rev. B* **70**, 104414 (2004).
 - 11 Y. Yoshida, S.-I. Ikeda, H. Matsuhata, N. Shirakawa, C. H. Lee, and S. Katano, *Phys. Rev. B* **72**, 054412 (2005).
 - 12 S. Nakatsuji, V. Dobrosavljević, D. Tanasković, M. Minakata, H. Fukazawa, and Y. Maeno, *Phys. Rev. Lett.* **93**, 146401 (2004).
 - 13 K. Takenaka, Y. Okamoto, T. Shinoda, N. Katayama, and Y. Sakai, *Nature Communications* **8**, 14102 (2017).
 - 14 O. Friedt, M. Braden, G. André, P. Adelman, S. Nakatsuji, and Y. Maeno, *Phys. Rev. B* **63**, 174432 (2001).
 - 15 M. Braden, G. André, S. Nakatsuji, and Y. Maeno, *Phys. Rev. B* **58**, 847 (1998).
 - 16 A. Jain, M. Krautloher, J. Porras, G. H. Ryu, D. P. Chen, D. L. Abernathy, J. T. Park, A. Ivanov, J. Chaloupka, G. Khaliullin, B. Keimer, and B. J. Kim, *Nat. Phys.* **13**, 633 (2017).
 - 17 S.-M. Souliou, J. Chaloupka, G. Khaliullin, G. Ryu, A. Jain, B. J. Kim, M. Le Tacon, and B. Keimer, *Phys. Rev. Lett.* **119**, 067201 (2017).
 - 18 L. Das, F. Forte, R. Fittipaldi, C. G. Fatuzzo, V. Granata, O. Ivashko, M. Horio, F. Schindler, M. Dantz, Y. Tseng, D. E. McNally, H. M. Rønnow, W. Wan, N. B. Christensen, J. Pelliciani, P. Olalde-Velasco, N. Kikugawa, T. Neupert, A. Vecchione, T. Schmitt, M. Cuoco, and J. Chang, *Phys. Rev. X* **8**, 011048 (2018).
 - 19 C. G. Fatuzzo, M. Dantz, S. Fatale, P. Olalde-Velasco, N. E. Shaik, B. Dalla Piazza, S. Toth, J. Pelliciani, R. Fittipaldi, A. Vecchione, N. Kikugawa, J. S. Brooks, H. M. Rønnow, M. Grioni, C. Rüegg, T. Schmitt, and J. Chang, *Phys. Rev. B* **91**, 155104 (2015).
 - 20 V. Bisogni, L. Simonelli, L. J. P. Ament, F. Forte, M. Moretti Sala, M. Minola, S. Huotari, J. van den Brink, G. Ghiringhelli, N. B. Brookes, and L. Braicovich, *Phys. Rev. B* **85**, 214527 (2012).
 - 21 M. Moretti Sala, M. Rossi, S. Boseggia, J. Akimitsu, N. B. Brookes, M. Isobe, M. Minola, H. Okabe, H. M. Rønnow, L. Simonelli, D. F. McMorrow, and G. Monaco, *Phys. Rev. B* **89**, 121101(R) (2014).
 - 22 X. Lu, P. Olalde-Velasco, Y. Huang, V. Bisogni, J. Pelliciani, S. Fatale, M. Dantz, J. G. Vale, E. C. Hunter, J. Chang, V. N. Strocov, R. S. Perry, M. Grioni, D. F. McMorrow, H. M. Rønnow, and T. Schmitt, *Phys. Rev. B* **97**, 041102(R) (2018).
 - 23 D. Pincini, L. S. I. Veiga, C. D. Dashwood, F. Forte, M. Cuoco, R. S. Perry, P. Bencok, A. T. Boothroyd, and D. F. McMorrow, *Phys. Rev. B* **99**, 075125 (2019).
 - 24 L. J. P. Ament, F. Forte, and J. van den Brink, *Phys. Rev. B* **75**, 115118 (2007).
 - 25 L. J. P. Ament, M. van Veenendaal, T. P. Devereaux, J. P. Hill, and J. van den Brink, *Rev. Mod. Phys.* **83**, 705 (2011).
 - 26 H. Fukazawa, S. Nakatsuji, and Y. Maeno, *Physica B* **281**, 613 (2000).
 - 27 S. Nakatsuji and Y. Maeno, *Journal of Solid State Chemistry* **156**, 26 (2001).
 - 28 G. Ghiringhelli, A. Piazzalunga, C. Dallera, G. Trezzi, L. Braicovich, T. Schmitt, V. N. Strocov, R. Betemps, L. Patthey, X. Wang, and M. Grioni, *Review of Scientific Instruments* **77**, 113108 (2006).
 - 29 V. Strocov, T. Schmitt, U. Flechsig, T. Schmidt, A. Imhof, Q. Chen, J. Raabe, R. Betemps, D. Zimoch, J. Krempasky, *et al.*, *Journal of synchrotron radiation* **17**, 631 (2010).
 - 30 C. T. Chen, L. H. Tjeng, J. Kwo, H. L. Kao, P. Rudolf, F. Sette, and R. M. Fleming, *Phys. Rev. Lett.* **68**, 2543 (1992).
 - 31 M. Malvestuto, E. Carleschi, R. Fittipaldi, E. Gorelov, E. Pavarini, M. Cuoco, Y. Maeno, F. Parmigiani, and A. Vecchione, *Phys. Rev. B* **83**, 165121 (2011).
 - 32 M. Malvestuto, V. Capogrosso, E. Carleschi, L. Galli, E. Gorelov, E. Pavarini, R. Fittipaldi, F. Forte, M. Cuoco, A. Vecchione, and F. Parmigiani, *Phys. Rev. B* **88**, 195143 (2013).
 - 33 E. B. Guedes, M. Abbate, K. Ishigami, A. Fujimori, K. Yoshimatsu, H. Kumigashira, M. Oshima, F. C. Vicentin, P. T. Fonseca, and R. J. O. Mossaneck, *Phys. Rev. B* **86**, 235127 (2012).
 - 34 A. Koga, N. Kawakami, T. M. Rice, and M. Sgrist, *Phys. Rev. Lett.* **92**, 216402 (2004).
 - 35 A. Liebsch and H. Ishida, *Phys. Rev. Lett.* **98**, 216403 (2007).
 - 36 E. Gorelov, M. Karolak, T. O. Wehling, F. Lechermann, A. I. Lichtenstein, and E. Pavarini, *Phys. Rev. Lett.* **104**, 226401 (2010).
 - 37 M. Braden, W. Reichardt, Y. Sidis, Z. Mao, and Y. Maeno, *Phys. Rev. B* **76**, 014505 (2007).
 - 38 H. Gretarsson, H. Suzuki, H. Kim, K. Ueda, M. Krautloher, B. J. Kim, H. Yavaş, G. Khaliullin, and B. Keimer, *Phys. Rev. B* **100**, 045123 (2019).
 - 39 T. Mizokawa, L. H. Tjeng, G. A. Sawatzky, G. Ghiringhelli, O. Tjernberg, N. B. Brookes, H. Fukazawa, S. Nakatsuji, and Y. Maeno, *Phys. Rev. Lett.* **87**, 077202 (2001).
 - 40 C. N. Veenstra, Z.-H. Zhu, M. Raichle, B. M. Ludbrook, A. Nicolaou, B. Slomski, G. Landolt, S. Kittaka, Y. Maeno, J. H. Dil, I. S. Elfimov, M. W. Haverkort, and A. Dama-

- scelli, *Phys. Rev. Lett.* **112**, 127002 (2014).
- ⁴¹ Q. Han and A. Millis, *Phys. Rev. Lett.* **121**, 067601 (2018).
- ⁴² D. Sutter, C. Fatuzzo, S. Moser, M. Kim, R. Fittipaldi, A. Vecchione, V. Granata, Y. Sassa, F. Cossalter, G. Gatti, M. Grioni, H. M. Rønnow, N. C. Plumb, C. E. Matt, M. Shi, M. Hoesch, T. K. Kim, T. R. Chang, H. T. Jeng, C. Jozwiak, A. Bostwick, E. Rotenberg, A. Georges, T. Neupert, and J. Chang, *Nat. Comm.* **8**, 15176 (2017).
- ⁴³ D. G. Porter, V. Granata, F. Forte, S. Di Matteo, M. Cuoco, R. Fittipaldi, A. Vecchione, and A. Bombardi, *Phys. Rev. B* **98**, 125142 (2018).
- ⁴⁴ Y. Wang, J. J. Wang, J. E. Saal, S. L. Shang, L.-Q. Chen, and Z.-K. Liu, *Phys. Rev. B* **82**, 172503 (2010).
- ⁴⁵ M. P. M. Dean, G. Dellea, R. S. Springell, F. Yakhou-Harris, K. Kummer, N. B. Brookes, X. Liu, Y.-J. Sun, J. Strle, T. Schmitt, L. Braicovich, G. Ghiringhelli, I. Božović, and J. P. Hill, *Nature Materials* **12**, 1019 EP (2013).
- ⁴⁶ C. Monney, T. Schmitt, C. E. Matt, J. Mesot, V. N. Strocov, O. J. Lipscombe, S. M. Hayden, and J. Chang, *Phys. Rev. B* **93**, 075103 (2016).
- ⁴⁷ J. Pelliciani, K. Ishii, Y. Huang, M. Dantz, X. Lu, P. Olalde-Velasco, V. N. Strocov, S. Kasahara, L. Xing, X. Wang, C. Jin, Y. Matsuda, T. Shibauchi, T. Das, and T. Schmitt, *Communications Physics* **2**, 139 (2019).
- ⁴⁸ F. Forte, M. Cuoco, and C. Noce, *Phys. Rev. B* **82**, 155104 (2010).
- ⁴⁹ M. Cuoco, F. Forte, and C. Noce, *Phys. Rev. B* **74**, 195124 (2006).
- ⁵⁰ M. Cuoco, F. Forte, and C. Noce, *Phys. Rev. B* **73**, 094428 (2006).
- ⁵¹ J. C. Slater and G. F. Koster, *Physical Review* **94**, 1498 (1954).
- ⁵² W. Brzezicki, C. Noce, A. Romano, and M. Cuoco, *Phys. Rev. Lett.* **114**, 247002 (2015).